The Astrophysical Journal, 945:15 (14pp), 2023 March 1 https://doi.org/10.3847/1538-4357/acabbc

Disentangling Modified Gravity and Massive Neutrinos with Intrinsic Shape Alignments of Massive Halos

Jounghun Lee[1], Suho Ryu[1], and Marco Baldi[2,3,4]
[1] Astronomy Program, Department of Physics and Astronomy, Seoul National University, Seoul 08826, Republic of Korea; cosmos.hun@gmail.com, jmhera2007@gmail.com
[2] Dipartimento di Fisica e Astronomia, Alma Mater Studiorum Università di Bologna, viale Berti Pichat, 6/2, I-40127 Bologna, Italy
[3] INAF—Osservatorio Astronomico di Bologna, via Ranzani 1, I-40127 Bologna, Italy
[4] INFN—Sezione di Bologna, viale Berti Pichat 6/2, I-40127 Bologna, Italy
Received 2022 June 7; revised 2022 November 16; accepted 2022 December 13; published 2023 March 1

Abstract

We present two new diagnostics based on the intrinsic shape alignments of group/cluster size dark matter halos to disentangle the effect of $f(R)$ gravity from that of massive neutrinos. Using snapshot data from a series of the DUSTGRAIN-pathfinder N-body simulations for a Planck ΛCDM cosmology and three $f(R)$ gravity models with massive neutrinos (ν), we first determine the probability density functions of the alignment angles between the shape orientations of massive halos and the minor principal axes of the local tidal fields. The numerically obtained results turn out to agree very well with the analytic formula derived under the assumption that the anisotropic merging along the cosmic web induces the halo shape alignments. The four cosmologies, which several standard diagnostics failed to discriminate, are found to yield significantly different best-fit values of the single parameter that characterizes their analytic formulae. We also numerically determine the spatial cross-correlations between the shape orientations of neighbor group/cluster halos, and find them to be in good agreements with a fitting formula characterized by two parameters, whose best-fit values are found to differ substantially among the four models. We also discuss the limitations and caveats of these new diagnostics that must be overcome for their application to real observational data.

Unified Astronomy Thesaurus concepts: Large-scale structure of the universe (902); Cosmology (343)

1. Introduction

If the scientific precept occam's razor were to be blindly used, then the standard ΛCDM cosmology based on Einstein's general relativity (GR) with a dominant cosmological constant (Λ) and cold dark matter (CDM) would win over all nonstandard ones since it is the simplest and most effective paradigm within which almost all observations can be explained (for a recent review, see Blanchard et al. 2022, and references therein). Nevertheless, the notorious fine-tuning problem of Λ (see Weinberg 1989; Carroll 2001, for reviews) has always left much room for us to come up with various alternatives in the faint hope that a more fundamental and natural description of the universe might become possible. Meanwhile, to survive multiple stringent observational tests, an alternative model must yield almost identical growth and expansion histories to the ΛCDM counterpart. In other words, the viability of an alternative cosmology is ensured only provided that it cannot be readily discriminated from the ΛCDM one by the conventional diagnostics based on the expansion and growth histories.

For instance, some $f(R)$ gravity models combined with massive neutrinos (ν) and CDM have been shown to be indistinguishable from ΛCDM cosmology by such powerful standard probes as the density power spectrum, evolution of the cluster abundance, and matter-to-halo bias factor (Baldi et al. 2014; Hagstotz et al. 2019). Here, $f(R)$ gravity is a modified gravity (MG) whose dynamics is described by the same Einstein–Hilbert action but with Ricci scalar, R, replaced by an arbitrary function, $f(R)$ (Buchdahl 1970; Starobinsky 1980; Hu & Sawicki 2007; Li & Barrow 2007). It predicts the presence of a fifth force in addition to gravity, but recovers GR in high-density environments via a screening mechanism called the chameleon (Khoury & Weltman 2004). The strength of a fifth force is quantified by the absolute value of its derivative, called the scalaron, at the present epoch, $|f_{R0}| \equiv |df/dR|_{z=0}$ (for a review, see Sotiriou & Faraoni 2010). The current observational constraint is $|f_{R0}| \lesssim 3.7 \times 10^{-6}$ on the cluster scale (e.g., Boubekeur et al. 2014).

However, if neutrinos (ν) have non-zero total mass, $M_\nu > 0$, then the observational data could allow $|f_{R0}|$ to have larger values than this constraint, since the presence of massive neutrinos would simultaneously suppress structure formation, thereby counteracting the enhancement due to the fifth force. Some combination of M_ν with $|f_{R0}|$ can beguile the standard diagnostics not to detect the presence of free streaming neutrinos and a fifth force by producing growth histories consistent with that of the standard ΛCDM case within observational uncertainties (Baldi et al. 2014). Breaking this *dark sector* degeneracy between the ΛCDM and the νCDM+$f(R)$ cosmologies requires an acutely sensitive nonlinear diagnostic that can perceive and react to a subtle difference between them in spite of their very similar growth and expansion histories. What has so far been proposed as such diagnostics includes the evolution of supercluster straightness, nonlinear growth rate, nonlinear redshift distortions, evolution of the drifting average coefficient of the isolated cluster abundance, high-order weak lensing statistics, and the high-redshift size distribution of cosmic voids (Giocoli et al. 2018;

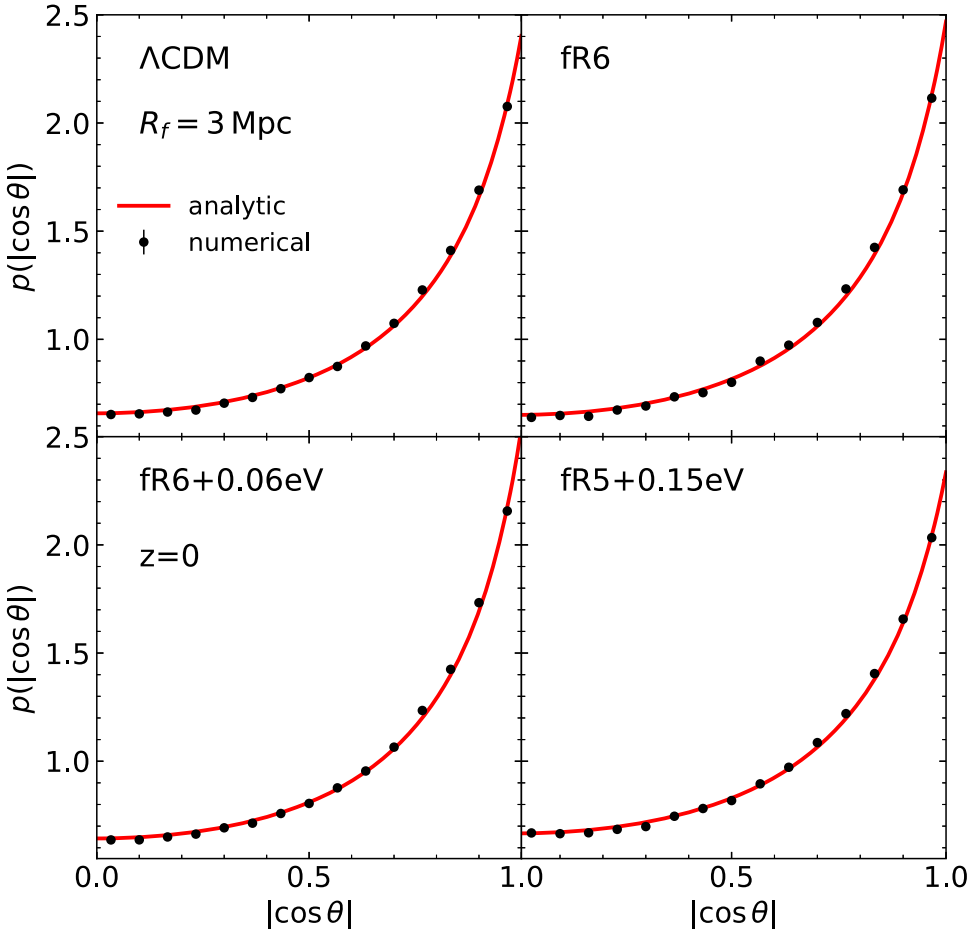

Figure 1. Numerically obtained probability density functions of the absolute values of the cosines of the angles between the cluster shapes and the directions of minimum matter compression (black filled circles with errors) compared with the analytic model with one best-fit parameter (red solid line), on the scale of $R_f = 3\,h^{-1}$ Mpc at $z = 0$ for the four different cosmologies.

Peel et al. 2018; Hagstotz et al. 2019; Wright et al. 2019; Ryu et al. 2020; Contarini et al. 2021).

Very recently, Chuang et al. (2022) suggested that the intrinsic shape alignment of galactic halos can be useful as a probe of gravity, showing by *N*-body simulations that its strength significantly differs between the ΛCDM and a $f(R)$ gravity model with $f_{R0} = 10^{-5}$ (fR5). Here, the intrinsic shape alignment of galactic halos refers to the phenomenon that the shape orientations of galactic halos exhibit a tendency of being preferentially aligned with the hosting filaments, which is believed to originate from the occurrence of anisotropic merging along the filamentary cosmic web (Altay et al. 2006; Hahn et al. 2007; Zhang et al. 2009, 2013; Chen et al. 2016; Lee 2019, and references therein). The fR5 model that Chuang et al. (2022) mainly considered, however, has been already well known to be readily distinguishable from ΛCDM cosmology by the aforementioned conventional diagnostics themselves (Baldi et al. 2014), since its growth and expansion histories significantly differ from that of ΛCDM cosmology. In other words, it is not a surprise that the strength of the intrinsic shape alignments of galactic halos differs between the ΛCDM and the fR5 models. A critical question that arises in light of Chuang et al. (2022)'s model is whether or not halo shape alignment could provide a new independent clue to the nature of gravity and DM beyond the constraints put by those standard statistics.

In this Paper, we intend to explore if the intrinsic shape alignments of group/cluster size halos can break the dark sector degeneracy between ΛCDM and νCDM+$f(R)$ cosmologies. We choose the group/cluster size halos rather than their galactic counterparts, since the shape orientations of those massive halos have long been well known to exhibit much stronger intrinsic alignments with the filaments (e.g., Altay et al. 2006; Hahn et al. 2007; Zhang et al. 2013; Lee 2019). The plan of this paper is as follows. In Section 2, we will briefly review the analytic prescriptions for the intrinsic shape alignments of DM halos with the tidal fields and present a new formula for the spatial correlations of the shape orientations of group/cluster halos. In Section 3, we will numerically examine if and how efficiently two new diagnostics based on the intrinsic shape alignments of group/cluster size halos can break the dark sector degeneracy among the ΛCDM and three different νCDM+$f(R)$ cosmologies. In Section 4, we will summarize the results and discuss the advantages and disadvantages of these new diagnostics compared with the conventional ones.

2. A Brief Review of the Analytic Model

Suppose that a DM halo is found at some position, $\boldsymbol{x}$, where the local tidal tensor, $\boldsymbol{T} = (T_{ij})$, smoothed on the scale of R_f, has three eigenvectors, $\{\boldsymbol{e}_1, \boldsymbol{e}_2, \boldsymbol{e}_3\}$, corresponding to three eigenvalues, $\{\lambda_1, \lambda_2, \lambda_3 | \lambda_1 \geqslant \lambda_2 \geqslant \lambda_3\}$. The eigenvectors, $\boldsymbol{e}_1$ and $\boldsymbol{e}_3$, are parallel to the directions of maximum and minimum matter compression, respectively. Since the sum of the three

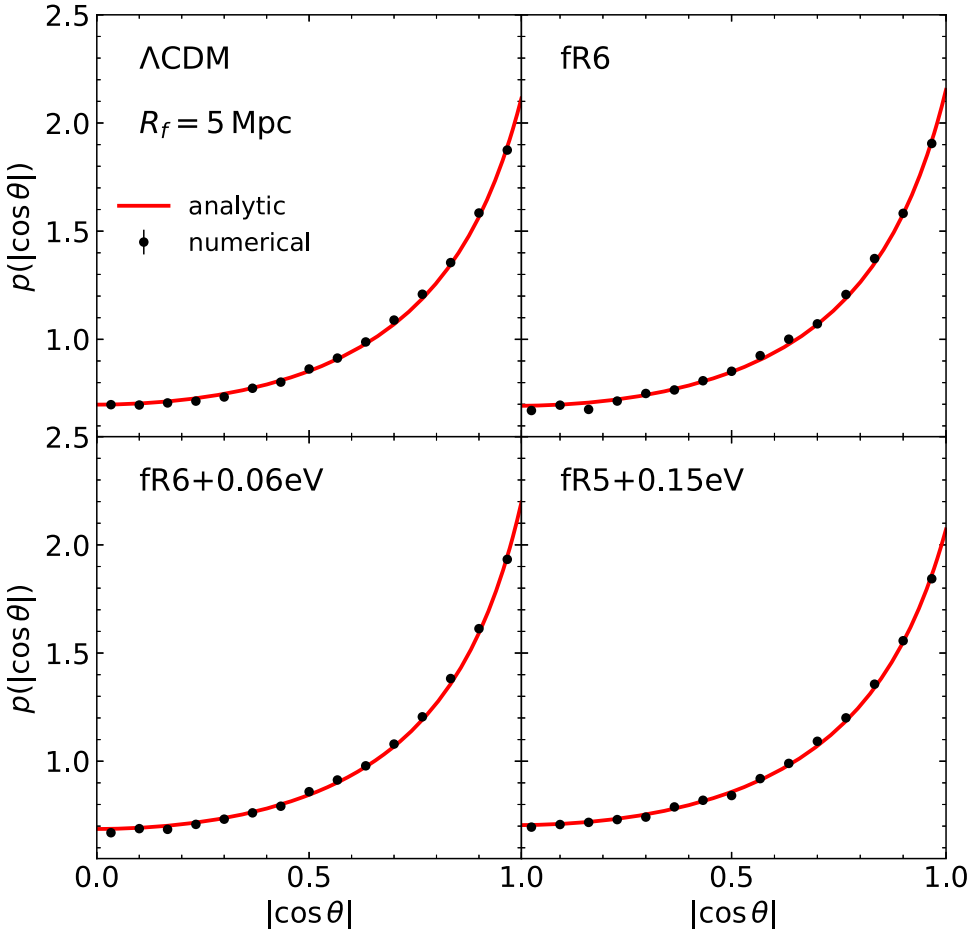

Figure 2. Same as Figure 1 but on the scale of $R_f = 5\,h^{-1}$ Mpc.

eigenvalues of $\boldsymbol{T}$ is equal to the local density, δ, the traceless tidal tensor, $\tilde{\boldsymbol{T}} = (\tilde{T}_{ij})$, can be obtained as $\tilde{T}_{ij} \equiv T_{ij} - (\delta/3)I_{ij}$, where I_{ij} is a 3×3 identity matrix. To single out only the anisotropic effect of the tidal field on the orientations of DM halo shapes, we will deal with $\hat{\boldsymbol{T}}$ rather than $\boldsymbol{T}$.

Suppose also that the DM halo has an ellipsoidal shape whose inertia momentum tensor, $\boldsymbol{U} = (U_{ij})$, has three eigenvalues and corresponding eigenvectors. Let $\hat{\boldsymbol{u}}$ denote a unit vector parallel to the major eigenvector of (U_{ij}) corresponding to its largest eigenvalue. We will refer to $\hat{\boldsymbol{u}}$ as the halo shape orientation throughout this paper. If a halo formed through an anisotropic merging along the cosmic web, its shape orientation, $\hat{\boldsymbol{u}}$, is expected to be in the direction of minimum matter compression. To describe quantitatively this expected alignment of $\hat{\boldsymbol{u}}$ with $\boldsymbol{e}_3$, Lee (2019) proposed the following analytic formula for the probability density function of $|\cos\theta| \equiv |\hat{\boldsymbol{u}} \cdot \hat{\boldsymbol{e}}_3|$:

$$p(|\cos\theta|) = \frac{1}{2\pi}\int_0^{2\pi}\left[\prod_{n=1}^{3}(1 + d_t - 3d_t\hat{\lambda}_n)\right]^{-\frac{1}{2}} \times \left(\sum_{l=1}^{3}\frac{|\hat{\boldsymbol{u}}\cdot\hat{\boldsymbol{e}}_l|}{1 + d_t - 3d_t\hat{\lambda}_l}\right)^{-\frac{3}{2}} d\phi. \quad (1)$$

Here, $\{\hat{\boldsymbol{e}}_1, \hat{\boldsymbol{e}}_2, \hat{\boldsymbol{e}}_3\}$ are the orthonormal eigenvectors of the unit traceless tidal tensor, $\hat{\boldsymbol{T}} \equiv \tilde{\boldsymbol{T}}/|\tilde{T}|$, in parallel to $\{\boldsymbol{e}_1, \boldsymbol{e}_2, \boldsymbol{e}_3\}$ corresponding to its three eigenvalues $\{\hat{\lambda}_1, \hat{\lambda}_2, \hat{\lambda}_3\,|\hat{\lambda}_1^2 + \hat{\lambda}_2^2 + \hat{\lambda}_3^2 = 1\}$, θ and ϕ are the spherical polar and azimuthal angles of $\hat{\boldsymbol{u}}$, respectively, in the principal frame of $\hat{\boldsymbol{T}}$, and d_t is an empirical parameter introduced to measure the strength of the $\hat{\boldsymbol{u}}$–$\hat{\boldsymbol{e}}_3$ alignment tendency. Lee (2019) showed that the best-fit value of d_t varies with R_f, reaching its maximum possible value when $R_f \equiv [3M/(4\pi\rho_m)]^{1/3}$, where ρ_m is the mean density of the universe and M is the halo mass. This optimal smoothing scale amounts to four times the halo virial radius, $R_f \sim 4r_{\rm vir}$ (Libeskind et al. 2013a).

If the shape orientations of DM halos are truly aligned with the direction of minimum matter compression parallel to $\hat{\boldsymbol{e}}_3$, then it is expected that the large-scale coherence of $\hat{\boldsymbol{T}}$ would induce shape–shape alignments between neighbor halos. Lee et al. (2008) defined the spatial cross-correlation function of $\hat{\boldsymbol{u}}$ as:

$$\eta(r) = \langle|\hat{\boldsymbol{u}}(\boldsymbol{x})\cdot\hat{\boldsymbol{u}}(\boldsymbol{x}+\boldsymbol{r})|^2\rangle - \frac{1}{3}, \quad (2)$$

where $\boldsymbol{r}$ is a separation vector and $1/3$ is the value of $\langle|\hat{\boldsymbol{u}}(\boldsymbol{x})\cdot\hat{\boldsymbol{u}}(\boldsymbol{x}+\boldsymbol{r})|^2\rangle$ in the asymptotic limit that $r \equiv \boldsymbol{r}/|\boldsymbol{r}|$ goes to infinity. The ensemble average in Equation (2) is to be taken over the halo pairs separated by the same distance, r.

The functional behavior of $\eta(r)$ should be closely linked with the spatial cross-correlations of the tidal fields, $C_{ijkl}(\boldsymbol{r}) \equiv \langle T_{ij}(\boldsymbol{x})T_{kl}(\boldsymbol{x}+\boldsymbol{r})\rangle$, the analytic expression for which was derived by Lee & Pen (2001) in the linear limit where $\boldsymbol{T}$ can be

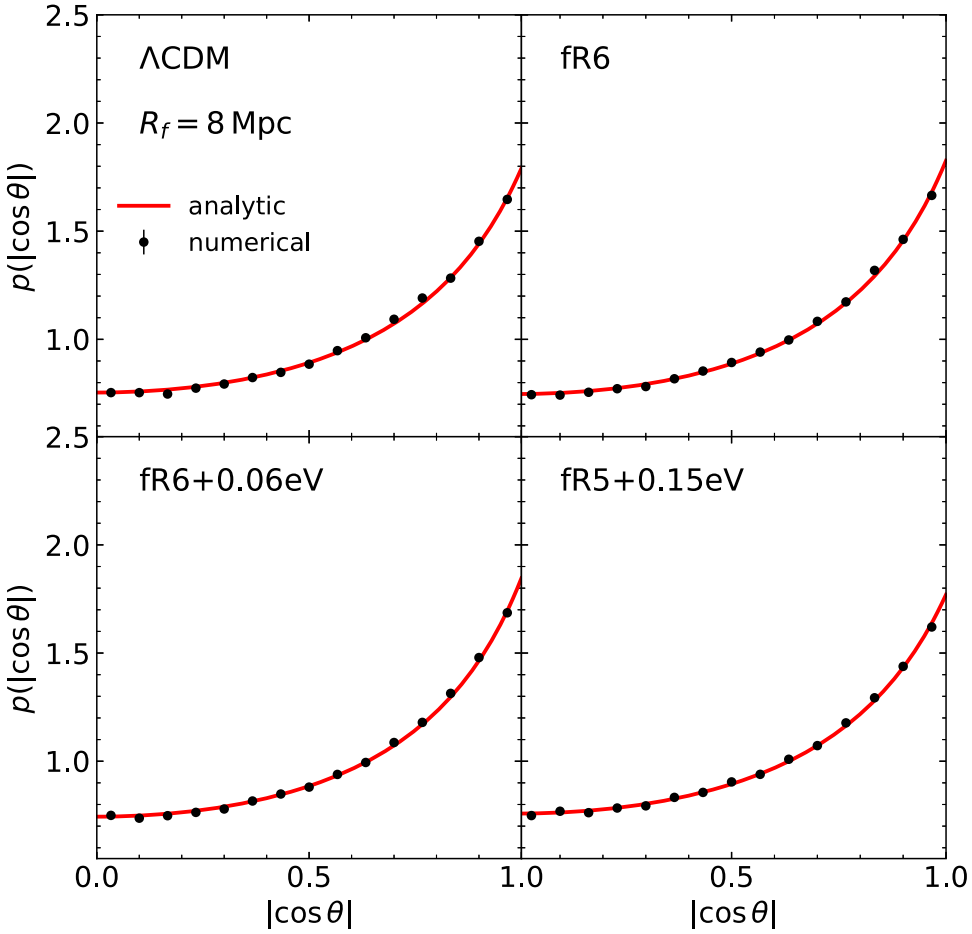

Figure 3. Same as Figure 1 but on the scale of $R_f = 8\,h^{-1}$ Mpc.

described as a Gaussian random field:

$$C_{ijkl}(\boldsymbol{r}) = (I_{ij}I_{kl} + I_{ik}I_{jl} + I_{il}I_{jk})\left\{\frac{J_3}{6} - \frac{J_5}{10}\right\} + (\hat{r}_i\hat{r}_j\hat{r}_k\hat{r}_l)\left\{\xi(r) + \frac{5J_3}{2} - \frac{7J_5}{2}\right\} + \frac{1}{2}(I_{ij}\hat{r}_k\hat{r}_l + I_{ik}\hat{r}_j\hat{r}_l + I_{il}\hat{r}_k\hat{r}_j + I_{jk}\hat{r}_i\hat{r}_l + I_{jl}\hat{r}_i\hat{r}_k + I_{kl}\hat{r}_i\hat{r}_j)\{J_5 - J_3\}. \quad (3)$$

Here, $\xi(r)$ is the two-point correlation function of the linear density field and $J_3(r)$ and $J_5(r)$ represent the third and fifth moments of $\xi(r)$, respectively, defined as (Lee & Pen 2001):

$$\xi(r) = \frac{1}{2\pi^2}\int_0^\infty P(k)W^2(k, R_f)\frac{\sin kr}{kr}k^2dk, \quad (4)$$

$$J_3(r) \equiv \frac{3}{r^3}\int_0^r \xi(r')r'^2dr'^2, \quad (5)$$

$$J_5(r) \equiv \frac{5}{r^5}\int_0^r \xi(r')r'^4dr'^4, \quad (6)$$

where $P(k)$ is the linear density power spectrum and $W(k, R_f)$ is the top-hat window function with a filtering radius of R_f. The spatial cross-correlations of the traceless tidal tensor, $\tilde{C}_{ijkl}(\boldsymbol{r}) \equiv \langle\tilde{T}_{ij}(\boldsymbol{x})\tilde{T}_{kl}(\boldsymbol{x}+\boldsymbol{r})\rangle$, can be obtained from Equation (3) as:

$$\tilde{C}_{ijkl}(\boldsymbol{r}) = C_{ijkl} - \frac{1}{3}I_{kl}C_{ijnn} - \frac{1}{3}I_{ij}C_{mmkl} + \frac{1}{9}I_{ij}I_{kl}C_{mmnn}. \quad (7)$$

Equation (7) reveals that the spatial correlation of $\tilde{\boldsymbol{T}}$ in the linear regime depends on the background cosmology through two linear quantities, $\xi(r)$ and $J_3(r) - J_5(r)$. If $\xi(r)$ behaved like a power-law function of r, then $\tilde{C}_{ijkl}$ would depend only on $\xi(r)$ since J_3 would be equal to J_5. The large-scale coherence of the anisotropic tidal field, which deviates $\xi(r)$ from the simple power-law scaling, plays the role of linking $\tilde{C}_{ijkl}$ to $J_3(r) - J_5(r)$.

Proposing an ansatz that the spatial cross-correlations of the halo shape orientations can be expressed in terms of $\xi(r)$ and $J_3(r) - J_5(r)$ like $\tilde{C}_{ijkl}$, we put forth the following two-parameter fitting formula for $\eta(r)$:

$$\eta(r) = g_1\frac{\xi(r; R_f)}{\sigma^2(R_f)} + g_2\left[\frac{J_3(r; R_f)}{\sigma^2(R_f)} - \frac{J_5(r; R_f)}{\sigma^2(R_f)}\right], \quad (8)$$

where $\sigma(R_f)$ is the rms fluctuation of the linear density field smoothed on the scale of R_f and g_1 and g_2 are two free parameters introduced to measure the strength of the cross-correlations of the halo shape orientations. The first parameter, g_1, measures the strength of the shape–shape alignments

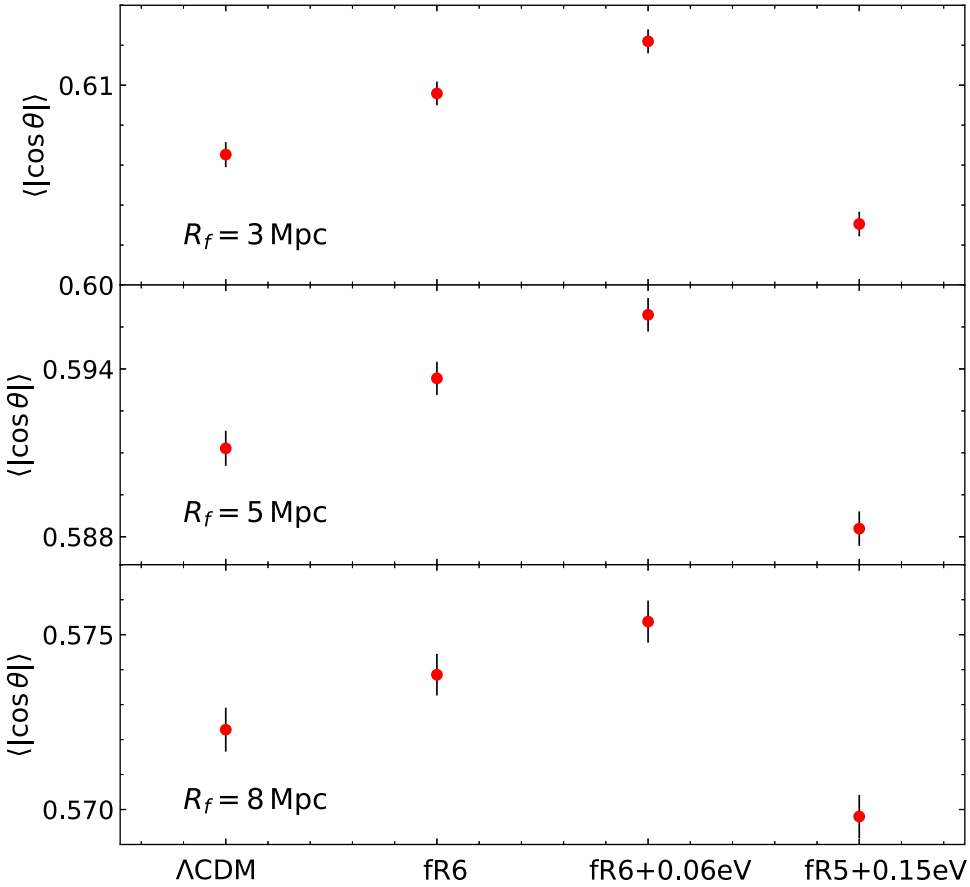

Figure 4. Numerically obtained mean absolute values of the cosines of the angles between the cluster shapes and the directions of minimum matter compression on three different scales for the four different cosmologies.

between the halos with comparable masses, while the second one, g_2, between the halos with different masses. Like d_t in Equation (1), these two parameters are expected to vary with the smoothing scale, having their maximum possible values on the scale of $R_f \sim 4r_{\rm vir}$ (Libeskind et al. 2013a).

3. Numerical Analysis

We utilize a data subset from the DUSTGRAIN-*pathfinder* project (Giocoli et al. 2018), a series of DM-only N-body experiments that simulated various νCDM+$f(R)$ cosmologies as well as a ΛCDM cosmology, with the help of the MG-GADGET code (Puchwein et al. 2013). For the DUSTGRAIN-*pathfinder* simulations, the widely applied Hu–Sawicki formula was used to specify $f(R)$ (Hu & Sawicki 2007), and the scheme developed by Viel et al. (2010) was applied to treat the massive neutrinos as hot DM particles. The linear box size ($L_{\rm box}$), the total number of DM particles ($N_{\rm par}$), and the particle mass resolution ($m_{\rm par}$) of the simulations are $L_{\rm box} = 750\,h^{-1}$ Mpc, $N_{\rm par} = 768^3$, and $m_{\rm par} = 8.1 \times 10^{10}\,h^{-1}\,M_\odot$, respectively. We refer the readers to Giocoli et al. (2018) and Puchwein et al. (2013) for full descriptions of the DUSTGRAIN-*pathfinder* project and the MG-GADGET code, respectively.

For our analysis, we consider the Planck ΛCDM (Planck Collaboration et al. 2016) and three different νCDM+$f(R)$ cosmologies, namely, fR6 with $|f_{R0}| = 10^{-6}$ and $M_\nu = 0.0$ eV, fR6 + 0.06 eV with $|f_{R0}| = 10^{-6}$ and $M_\nu = 0.06$ eV, and fR5 + 0.15 eV with $|f_{R0}| = 10^{-5}$ and $M_\nu = 0.15$ eV. These three νCDM+$f(R)$ models have been known to be highly degenerate with the Planck ΛCDM cosmology by the standard diagnostics based on the growth history (Baldi et al. 2014; Hagstotz et al. 2019). Especially, the fR6 + 0.06 eV and ΛCDM pair shares an identical normalization amplitude of the linear density power spectrum, σ_8, while the fR5 + 0.15 eV and fR6 pair exhibits a negligibly small difference in σ_8 between each other (see Table 1).

Table 1
Numbers of Selected Group/Cluster Halos for each Cosmology

Model	$\lvert f_{R0}\rvert$	$\sum m_\nu$ (eV)	σ_8	$N_{8.1}$	$N_{10.1}$	$N_{\rm sync}$
ΛCDM	⋯	0.0	0.847	217567	159969	208500
fR6	10^{-6}	0.0	0.861	242418	176106	208500
fR6+0.06eV	10^{-6}	0.06	0.847	238003	173164	208500
fR5+0.15eV	10^{-5}	0.15	0.864	226161	168259	208500

For each of the four cosmologies, we apply the Rockstar algorithm (Behroozi et al. 2013) to the DM particle snapshot at $z = 0$ to obtain a catalog of DM halos which lists a variety of their properties such as their position ($\boldsymbol{x}$), virial mass (M), and shape. Basically, the method devised by Allgood et al. (2006) was incorporated into the Rockstar algorithm to determine the ellipsoidal shape of a DM halo, providing information on the direction of the shape orientation of each halo, $\hat{\boldsymbol{u}}$, as well as on the intermediate-to-major axial ratio, p. Applying a mass cut of $M_{\rm cut} = 8.1 \times 10^{12}\,h^{-1}\,M_\odot$ and an axial ratio cut of $p_{\rm cut} = 0.9$ to the virial mass and intermediate-to-major axial ratios, we make a selection of massive triaxial distinct halos without being

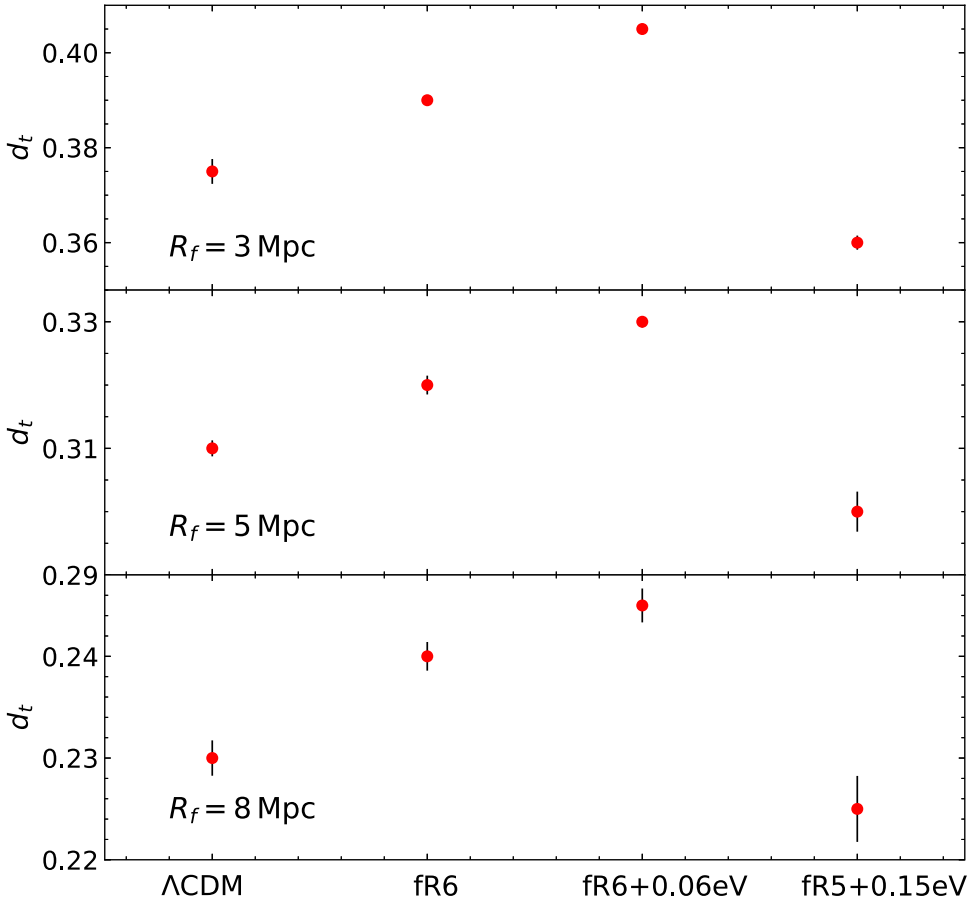

Figure 5. Best-fit values of the shape correlation parameter on three different scales for the four different cosmologies.

embedded in any larger halos. These two conditions are to ensure a relatively high degree of accuracy in the determination of the shape orientations of the selected halos.[5] The fifth column of Table 1 also shows the number of selected massive halos, $N_{8.1}$, for each model. Employing the $\boldsymbol{T}$-reconstruction routine described by Lee (2019), we determine the unit traceless tidal tensor, $\hat{\boldsymbol{T}}$, smoothed on the scale of R_f at the position of each selected halo. Via the similarity transformation, we find three eigenvalues, $\hat{\lambda}_1$, $\hat{\lambda}_2$, $\hat{\lambda}_3$, and corresponding eigenvectors, $\hat{\boldsymbol{e}}_1$, $\hat{\boldsymbol{e}}_2$, and $\hat{\boldsymbol{e}}_3$ of $\hat{\boldsymbol{T}}$ (see also Lee et al. 2021).

For each selected halo, we calculate $|\cos\theta| \equiv |\hat{\boldsymbol{u}} \cdot \hat{\boldsymbol{e}}_3|$. Splitting the range of $0 \leqslant |\cos\theta| \leqslant 1$ into twelve short bins of equal length, $\Delta\cos\theta$, and counting the numbers of those halos whose values of $|\cos\theta|$ fall in each bin, ΔN, we numerically determine the probability density function, $p(|\cos\theta|) = \Delta N/(\Delta\cos\theta \times N_{\rm tot})$, where $N_{\rm tot}$ denotes the total number of selected massive halos at $z = 0$. Plugging the mean values of $\hat{\lambda}_1$, $\hat{\lambda}_2$, $\hat{\lambda}_3$ averaged over the selected halos into Equation (1), we fit the analytic formula to the numerical results with Poissonian errors by adjusting the parameter d_t via $\chi^2(d_t)$-minimization. The error in d_t is calculated as one standard deviation, σ_{d_t}, from the maximum likelihood distribution, $p(d_t) \propto \exp[-\chi(d_t)^2/2]$.

Figure 1 plots the numerically obtained $p(|\cos\theta|)$ (black filled circles) with Poisson errors as well as the analytic formula, Equation (1), with the best-fit parameter (red solid line) on the scale of $R_f = 3\,h^{-1}$ Mpc at $z = 0$ for the four different cosmological models. This choice of $R_f = 3\,h^{-1}$ Mpc is made by compromising between the particle resolution of the simulations and the validity of Equation (1). As can be seen, all of the four models exhibit the existence of strong $\hat{\boldsymbol{u}}$–$\hat{\boldsymbol{e}}_3$ alignments, but differ from one another in the functional behavior of $p(|\cos\theta|)$, which is excellently described by the analytic formula with the best-fit value of d_t. We also repeat the same calculation for two different cases of the smoothing scales, $R_f = 5\,h^{-1}$ Mpc and $8\,h^{-1}$ Mpc, the results of which are shown Figures 2–3, respectively. The good agreements between the numerical and analytical results seem to be robust against the variation of R_f. For a given cosmology, however, the $\hat{\boldsymbol{u}}$–$\hat{\boldsymbol{e}}_3$ alignment becomes stronger for the case where the tidal field is smoothed on the smaller scale, inconsistent with what Lee (2019) found for the ΛCDM case.

Figures 4 and 5 show how significantly the four models differ from one another in the ensemble average, $\langle|\cos\theta|\rangle$, and in the best-fit value of d_t, respectively, for the three cases of R_f. Note that the single parameter, d_t, of the analytic formula varies more strongly with the four models than $\langle|\cos\theta|\rangle$, demonstrating the efficiency of the analytic formula in distinguishing among the four models. The success of Equation (1) in matching the numerical results and its efficiency in

[5] As shown by Allgood et al. (2006), the minimum number of particles, 1000, corresponding to the mass cut of $M_{\rm cut} = 8.1 \times 10^{13}\,h^{-1}\,M_\odot$ in the current analysis, is in fact required to ensure a negligible degree of numerical contamination in the determination of the halo shapes. However, the current analysis cannot afford to this high value of $M_{\rm cut}$ since the number of the halos would drastically drop due to the relatively low particle resolution of the simulations.

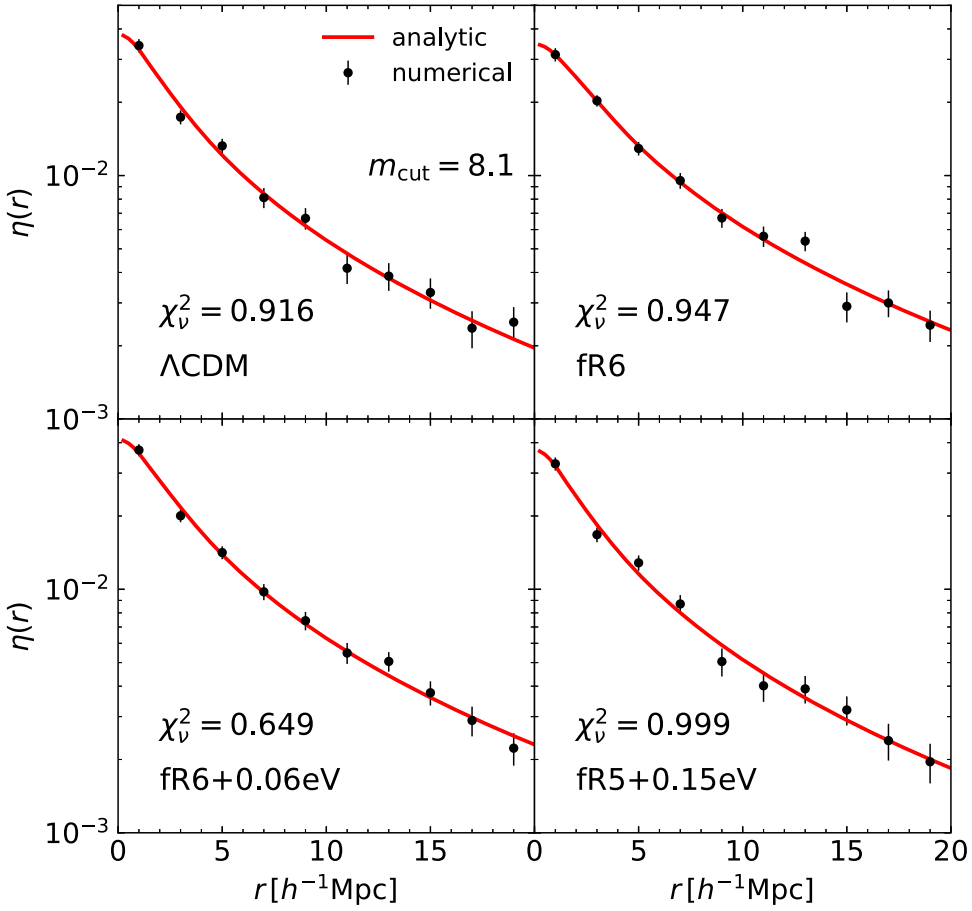

Figure 6. Numerically obtained halo shape–shape cross-correlation functions (black filled circles) compared with the analytic model with the two best-fit parameters (red solid curves) for the four different cosmologies at $z = 0$.

discriminating degenerate models implies that the nature of gravity and DM must leave a unique imprint on the shape orientations of group/cluster halos relative to the large-scale tidal fields by modulating the anisotropic occurrence of the merger events along the cosmic web.

Our explanation for the nonmonotonic or incoherent change of d_t with $|f_R|$ and $\sum m_\nu$, is as follows. The strength of the shape alignments of group/cluster halos with the tidal field is determined not only by how rapidly the density fluctuations grow but also by how anisotropic the large-scale cosmic web becomes in the nonlinear regime. The incoherent change of d_t simply reflects the fact that the strength of this alignment is the consequence of the delicate counterbalance between the two effects. The high value of $|f_R|$ enhances the density growth, spurring the hierarchical merging, which can enhance the shape alignments. But, at the same time, the high value of $|f_R|$ makes the cosmic web less anisotropic (i.e., more isotropic), which can weaken the shape alignments. Similarly, the high value of $\sum m_\nu$ can have similar dual effects on the shape alignments since the presence of more massive neutrinos can suppress more severely the density growth, deterring the hierarchical merging process, while it can also make the cosmic web more anisotropic.

The monotonic increase of d_t as the background changes from the ΛCDM to the fR6 + 0.06 eV model implies that in these ranges of $0 \leqslant |f_R| \leqslant 10^{-6}$ and $0 \leqslant \sum m_\nu/\mathrm{eV} \leqslant 0.06$, the gravity and neutrinos are strong and massive enough, respectively, to have an enhancing effect on the shape alignments. The lowest value of d_t exhibited by the fR5 + 0.15 eV model implies that at these high values of $|f_R| = 10^{-5}$ and $\sum m_\nu/\mathrm{eV} = 0.15$, the gravity and neutrinos are so strong and so massive, respectively, that they have the opposite effect of reducing the shape alignments. This incoherent variation of d_t with $|f_R|$ and $\sum m_\nu$ is in fact a manifestation of its potential to discriminate degenerate cosmological models, which both of the linear and nonlinear density correlations fail to achieve. In other words, our statistic can complement the other conventional diagnostics based on the density growth history since it brings out a different aspect of the nonlinear evolution of the halos in the cosmic web—depending not only on how fast the halos grow but also on how anisotropic merging process the halos undergo.

Although it turns out that $p(|\cos\theta|)$ is very powerful in principle to distinguish among degenerate models, the practical success of this statistic is contingent upon the availability of prior information on the background cosmology for the reconstruction of the real-space tidal fields. Another diagnostic based on the shape orientations of DM halos, which does no require such prior information, is its spatial cross-correlation, $\eta(r)$. For the numerical determination of $\eta(r)$, we calculate the separation distance, r, between each pair of selected halos with shape orientations, say, $\hat{\boldsymbol{u}}_1$ and $\hat{\boldsymbol{u}}_2$. Dividing the range of r into multiple bins of equal length $\Delta r = 2\,h^{-1}$ Mpc, we compute the ensemble average, $\langle|\hat{\boldsymbol{u}}_1 \cdot \hat{\boldsymbol{u}}_2|^2 - 1/3\rangle$, over halo pairs whose separation distances fall in $[r, r + \Delta r]$ to obtain $\eta(r)$. Then, we create 1000 bootstrap resamples of the halo pairs falling in each

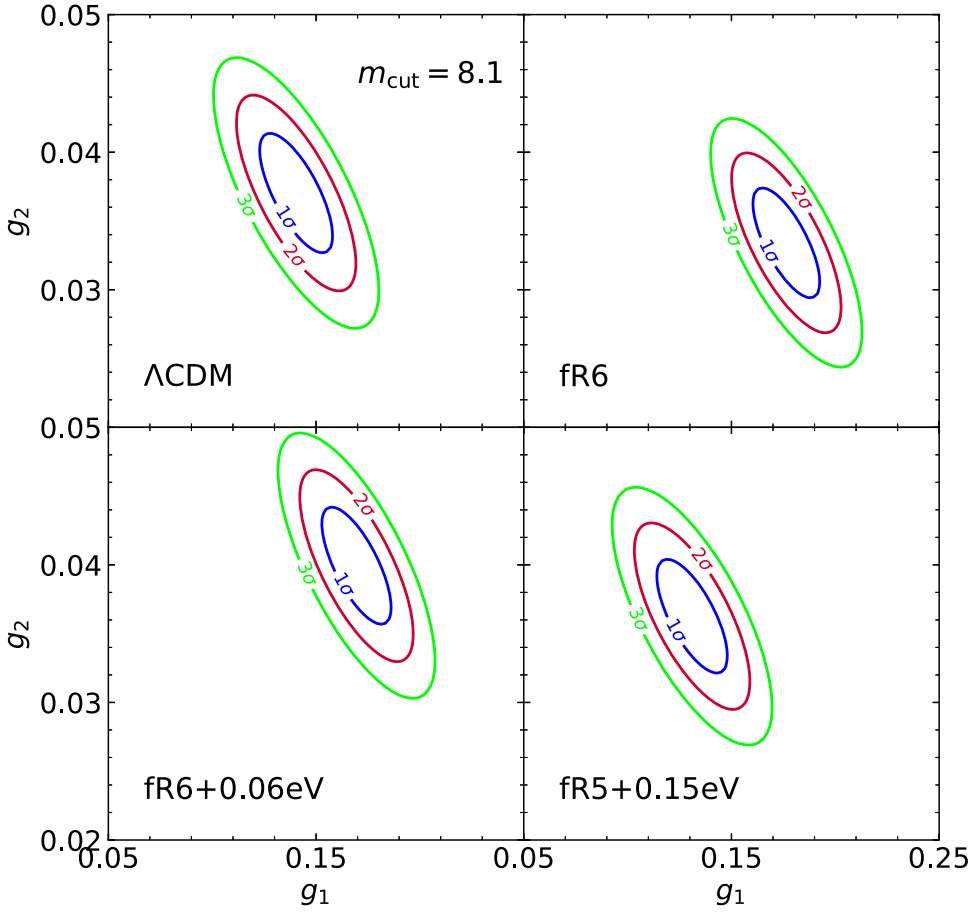

Figure 7. 68%, 95%, and 99% confidence regions of the χ^2-values in the configuration space spanned by the two shape correlation parameters.

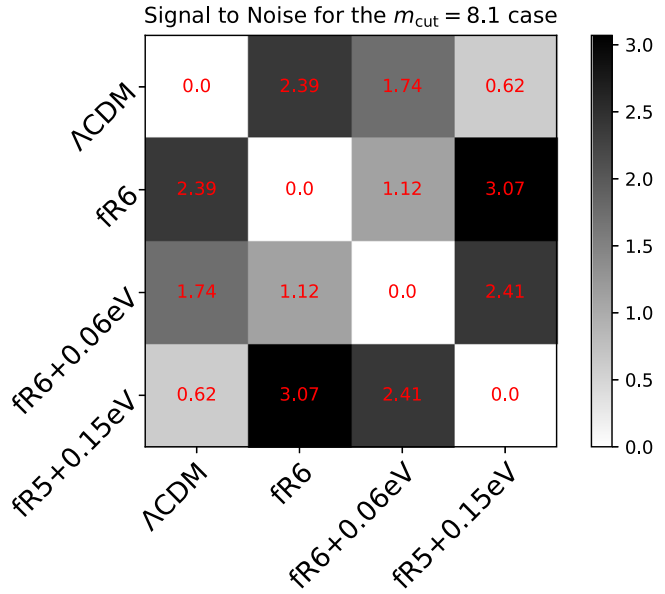

Figure 8. Signal-to-noise ratios of the differences among the ΛCDM, fR6, fR6 + 0.06 eV, and fR5 + 0.15 eV cosmologies.

of the r bins, and calculate the one standard deviation scatter among the resamples as the associated error, σ_η.

The analytic formula for $\eta(r)$, Equation (8), is fitted to the numerically obtained $\eta(r)$ by adjusting two parameters, g_1 and g_2, via $\chi^2(g_1, g_2)$-minimization. To evaluate $\xi(r)$, $J_3(r)$, and $J_5(r)$ in Equation (8), we consistently use the same linear density power spectrum of the Planck ΛCDM model for all of the four models, mimicking the realistic situation where no prior information regarding the background cosmology is available. If $\eta(r)$ is truly a powerful discriminator of nonstandard models, then the best-fit values of g_1 and g_2 would significantly differ among the four models, despite the same linear density power spectrum being consistently used to evaluate the analytic formula.

Figure 6 plots the numerically derived $\eta(r)$ (black filled circles) at $z = 0$ as well as the analytic formula (red solid line) with the best-fit parameters, g_1 and g_2, for the four models. It also shows the values of the reduced χ^2, i.e., $\chi^2_\nu \equiv \chi^2/n_f$, where n_f denotes the degrees of freedom equal to the number of bins subtracted by 2, the number of free parameters. As can be seen, for each model, we detect a clear signal of strong spatial cross-correlation of the halo shape orientations over a large distance up to $20\,h^{-1}$ Mpc, and find good agreement between the numerical results and the analytic formula with the best-fit parameters for all of the four models. Figure 7 plots the 68%, 95%, and 99% contours of $\chi^2(g_1, g_2)$ for the four models.

The statistical differences in $\eta(r)$ between two degenerate models can be effectively quantified by measuring the distances in the configuration space spanned by the two aforementioned parameters. Let $\{g_1, g_2, \sigma_{g_1}, \sigma_{g_2}, \sigma_{g_1 g_2}\}$ and $\{g_1', g_2', \sigma_{g_1'}, \sigma_{g_2'}, \sigma_{g_1' g_2'}\}$ denote two sets of the first and second best-fit parameters of η, their marginalized errors, and the covariance between them for the two models, respectively, which can be all obtained from the numerically obtained posterior distributions $p[-\chi^2(g_1, g_2)/2]$. Defining the distance

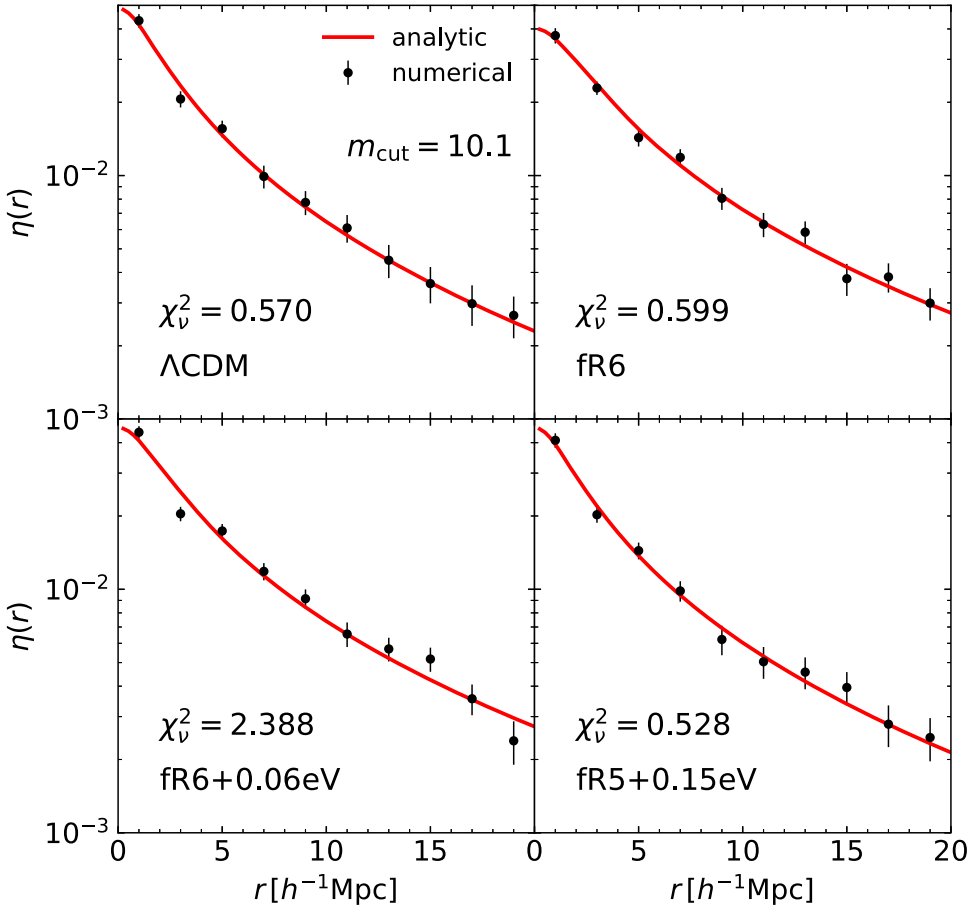

Figure 9. Same as Figure 6 but for the case of a higher mass cut, $10.1 \times 10^{12}\,h^{-1}\,M_\odot$, is applied.

D between them as $D \equiv [(g_1 - g_1')^2 + (g_2 - g_2')^2]^{1/2}$, we determine the associated errors by the following error propagation formula as:

$$\sigma_D^2 = \left(\frac{\partial D}{\partial g_1}\right)^2 \sigma_{g_1}^2 + \left(\frac{\partial D}{\partial g_2}\right)^2 \sigma_{g_2}^2 + \left(\frac{\partial D}{\partial g_1'}\right)^2 \sigma_{g_1'}^2 + \left(\frac{\partial D}{\partial g_2'}\right)^2 \sigma_{g_2'}^2 + 2\left(\frac{\partial D}{\partial g_1}\right)\left(\frac{\partial D}{\partial g_2}\right)\sigma_{g_1 g_2} + 2\left(\frac{\partial D}{\partial g_1'}\right)\left(\frac{\partial D}{\partial g_2'}\right)\sigma_{g_1' g_2'}. \quad (9)$$

Figure 8 plots D/σ_D for each pair of the four cosmologies. The two degenerate models, fR6 and fR5 + 0.15 eV, yield the highest signal-to-noise ratio, $D/\sigma_D \gtrsim 3$, while the other two degenerate models, ΛCDM and fR6 + 0.06 eV, produce only a 1.74 signal-to-noise ratio. Note also that the substantial signal-to-noise ratios are found from the other two pairs: $D/\sigma_D = 2.39$ ($D/\sigma_D = 2.41$) for the ΛCDM and fR6 (fR6 + 0.06 eV and fR5 + 0.15 eV) models.

To see if the result would depend on our specific choice of $M_{\rm cut}$ for the selection of the halos, we repeat the whole analysis but with a higher mass cut, $M_{\rm cut} = 10.1 \times 10^{12}\,h^{-1}\,M_\odot$. The number of the halos, $N_{10.1}$, selected by applying this higher mass cut for each model is provided in the sixth column of Table 1. Figures 9–11 plot the same as Figures 6–8 but from the halos selected by applying $M_{\rm cut} = 10.1 \times 10^{12}\,h^{-1}\,M_\odot$, respectively. As can be seen from Figure 9, the analytic formula, Equation (8), still works quite well in describing the numerical results, demonstrating its robustness against the variation of $M_{\rm cut}$. A comparison of Figure 7 with Figure 10 also proves the consistency in the trends of the two parameters with the four models, except for the contour sizes, in spite of the change of $M_{\rm cut}$. Figure 11 reveals that this new statistic based on η is in principle capable of breaking the degeneracy between the fR6 and fR5 + 0.15 eV models, still producing a significant signal-to-noise ratio, $D/\sigma_D > 3$.

There is, however, one more test that $\eta(r)$ must pass for its validity to be confirmed as a discriminator of degenerate cosmologies. Even though the mass and axial ratio distributions of the four degenerate models are quite similar to one another, they are not identical. Since the shape–shape correlations are strongly dependent on the halo mass and axial ratios, it should be necessary to inspect whether or not the detected difference in $\eta(r)$ among the degenerate models are due to differences in the mass and axial ratio distributions. For this inspection, we control the halo samples from the four models so that they share identical mass and axial ratio distributions. The seventh column of Table 1 also lists the total number of halos, $N_{\rm sync}$, belonging to the controlled samples for each model. Figures 12–13 plot the number counts of the halos as a function of their mass and axial ratios, respectively, from the original (top panel) and controlled (bottom panel) subsamples. As can be seen, the small but nonnegligible differences in the mass and axial ratio distributions among the four models disappear as the controlled subsamples replace the original ones.

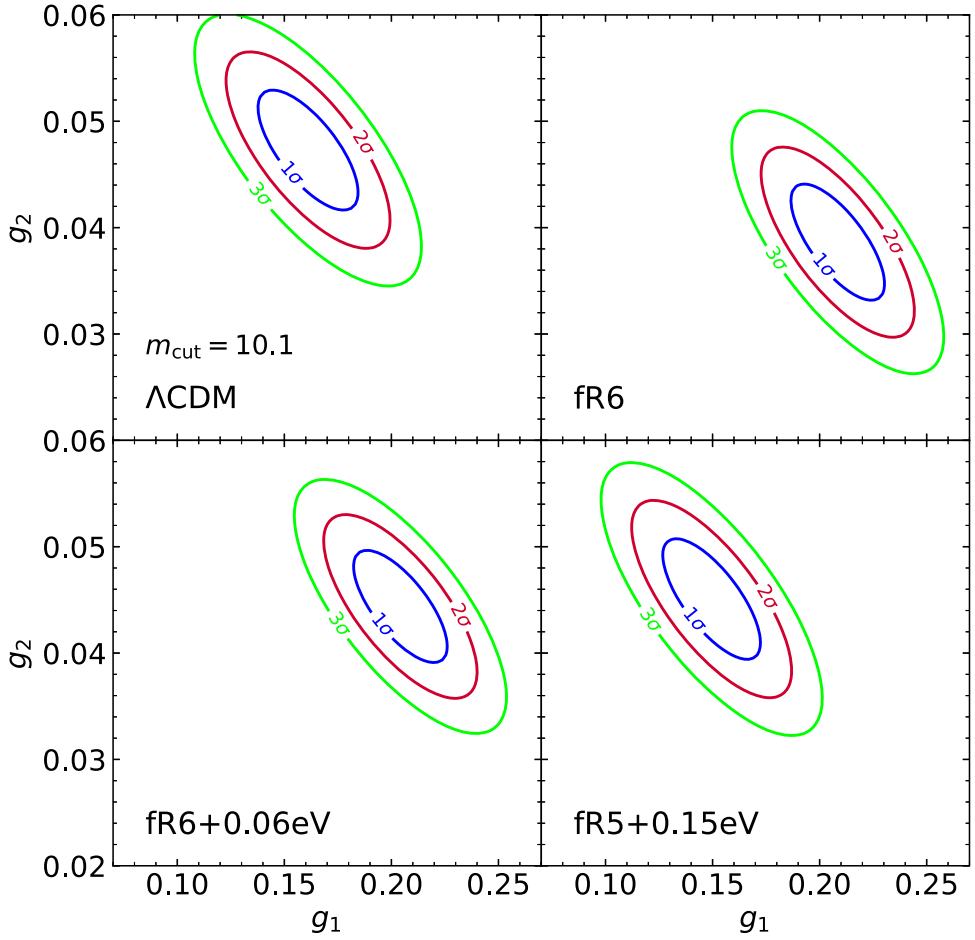

Figure 10. Same as Figure 7 but for the case of a higher mass cut, $10.1 \times 10^{12}\,h^{-1}\,M_{\odot}$, is applied.

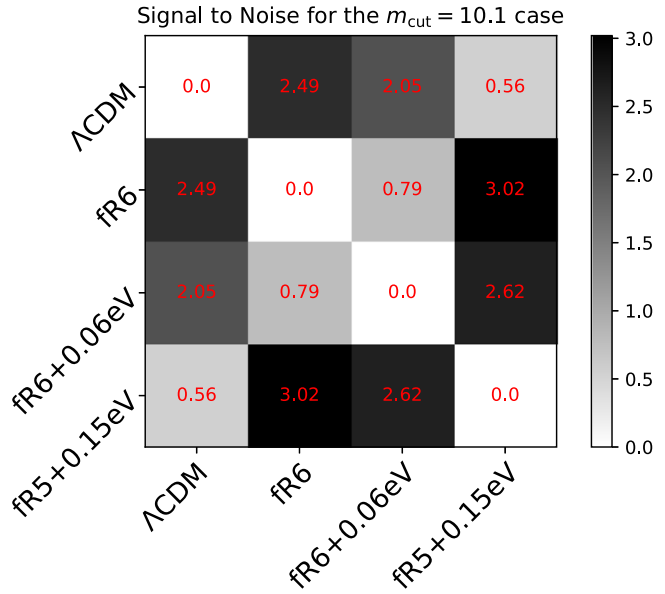

Figure 11. Same as Figure 8 but for the case of a higher mass cut, $10.1 \times 10^{12}\,h^{-1}\,M_{\odot}$, is applied.

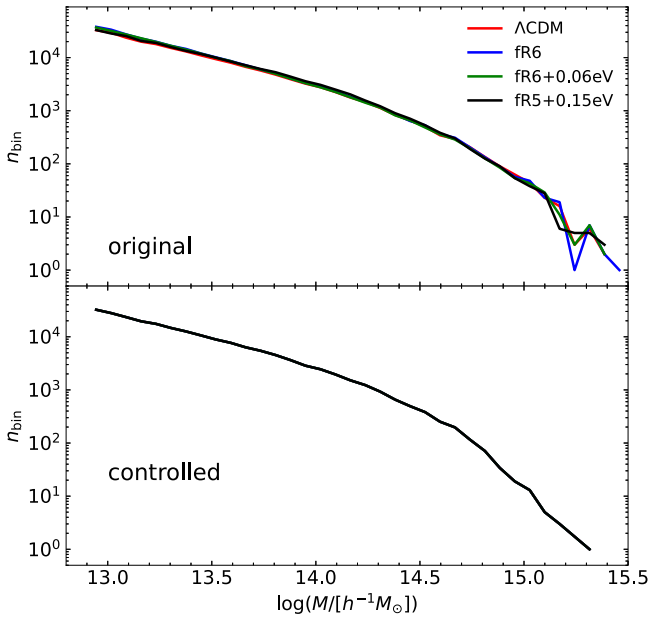

Figure 12. Number distributions of the halos belonging the original (top panel) and controlled (bottom panel) samples from the four models as a function of halo mass.

Figures 14–16 plot the same as Figures 6–8 but for the controlled subsamples. As can be seen, the signal-to-noise ratios from the controlled samples diminish down to insignificant values for all of the cases. The highest value of D/σ_D is found to be 2.56 from the fR6 and fR5 + 0.15 eV pair, while the other degenerate pairs, ΛCDM and fR6 + 0.06 eV yield only 1.49. Nonetheless, we suspect that these lower values of D/σ_D should be ascribed to the much smaller sizes of the

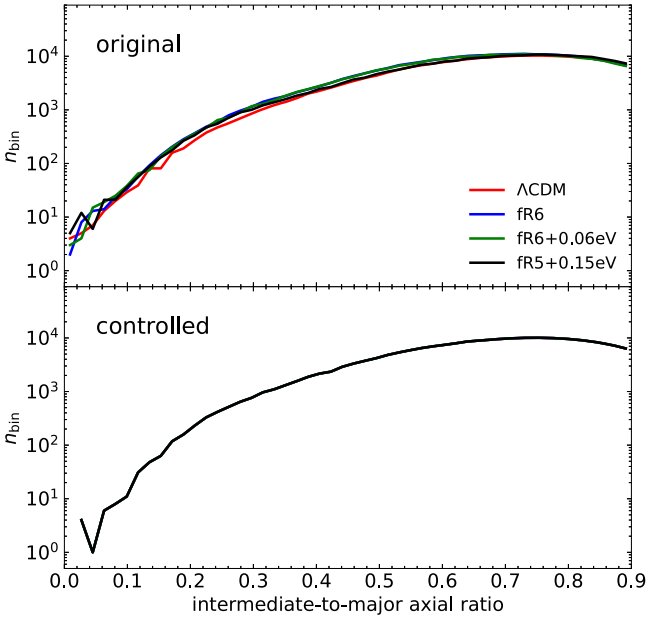

Figure 13. Number distributions of the halos belonging the original (top panel) and controlled (bottom panel) samples from the four models as a function of halo axial ratio.

controlled samples compared with the original ones (see Table 1), noting that the trends of the variation of $\eta(r)$ and its two parameters with the four models seem to be robust, insensitive to whether or not the samples are original or controlled.

4. Summary and Conclusion

We have put forth two diagnostics based on the shape orientations of group/cluster halos to break the dark sector degeneracy between standard ΛCDM and nonstandard νCDM+$f(R)$ cosmologies. One is the statistical tendency of the halo shape orientations being preferentially aligned with the directions of minimum matter compression in parallel to the minor principal directions of the linearly reconstructed tidal fields, while the other is their spatial cross-correlations. Analysing data subsets from the DUSTGRAIN-*pathfinder* simulations performed for the ΛCDM, fR6, fR6 + 0.06 eV, and fR5 + 0.15 eV cosmologies, we have determined the first diagnostics at $z = 0$. The numerical results have been compared with the analytic single parameter formula developed by Lee (2019) under the assumption that the intrinsic shape alignments of the DM halos originate from the anisotropic occurrence of merging events along the cosmic web (e.g., West 1994; Faltenbacher et al. 2002; Kasun & Evrard 2005; Libeskind et al. 2013b; Wittman et al. 2019, and references therein).

Finding an excellent agreement between the analytical and numerical results, we have shown that the best-fit parameter of the analytic formula very effectively quantifies the significant differences in the alignment strengths between the degenerate models. The difference in the best-fit value of the parameter has turned out to be as significant as 6σ (10σ) between the ΛCDM and fR6 + 0.06 eV (between the fR6 and fR5 + 0.15 eV) cosmologies, despite the two models sharing almost the same growth histories and same normalization amplitudes of their linear density power spectra. It has been also confirmed that this result, the success of the analytic formula and its potential to discriminate degenerate models from each other, is robust against variations of the smoothing scale of the tidal fields from $R_f = 3$ to $8\,h^{-1}$ Mpc.

Meanwhile, expecting that the large-scale coherence of the linear tidal fields would induce the shape orientations of the massive halos to be spatially cross-correlated (West 1994; Onuora & Thomas 2000; Faltenbacher et al. 2002; Kasun & Evrard 2005; Altay et al. 2006; Smargon et al. 2012), we have devised a two-parameter formula expressed in terms of the linear density two-point correlation function and its third and fifth moments for the halo shape–shape correlation. It has been found that the differences in the two best-fit parameters are as substantial as $\sim 1.49\sigma_D$ ($\sim 2.56\sigma_D$) between the ΛCDM and fR6 + 0.06 eV (between the fR6 and fR5 + 0.15 eV) cosmologies, when no prior information on the background cosmology has been used to evaluate the analytic formula and the halo samples have been controlled to have identical mass and axial ratio distributions. This result indicates a much larger sample of group and cluster halos will be required to test the potential of the second diagnostic as cosmological discriminators.

It is worth discussing why we have utilized the massive group/cluster halos rather than the galactic counterparts as the main targets for these new diagnostics. In the original work of Chuang et al. (2022), who for the first time suggested the halo intrinsic shape alignments as a test of $f(R)$ gravity, their analysis was made exclusively on the galactic scale under the assumption that the intrinsic shape alignments of galactic halos are observable since the shape orientations of the DM components of galactic halos should be well aligned with those of their observable stellar components. However, a recent numerical analysis based on high-resolution hydrodynamical simulations revealed that this assumption cannot be justified on the galactic scale, witnessing significant misalignments between the shape orientations of the DM and stellar components of the galactic halos (Lee & Moon 2022). The same numerical analysis also revealed that the hot gas and DM components exhibited strong shape alignments with each other and that the alignments become stronger on larger mass scales. Given these numerical clues along with the fact that the shape orientations of galaxy groups and clusters are often determined from the distributions of their hot gas components (e.g., Zaroubi et al. 2001), the intrinsic shape alignments of the group/cluster halos should be a better indicator of the nature of gravity and DM than those of the galactic halos.

Although galaxy groups/clusters are much less abundant than galaxies, which is likely to cause larger statistical errors, another merit of using them as the main targets is that their shape orientations reflect much better the anisotropic merging along the large-scale filamentary web (Altay et al. 2006; Hahn et al. 2007). The analytic formulae expressed in terms of the linear quantities must work better in approximating the intrinsic spin alignments and spatial correlations on the group and cluster scales (Lee 2019) than on the galactic scales. Moreover, our diagnostics require only single redshift observations at $z = 0$, unlike the previously suggested probes to break the dark sector degeneracy, like the nonlinear growth rate, nonlinear redshift distortions, evolution of the drifting average coefficient of the isolated cluster abundance, high-order weak lensing statistics, and high-redshift size distribution of cosmic voids, all of which require multiple redshift observations (e.g., Giocoli et al. 2018; Peel et al. 2018; Hagstotz et al. 2019; Wright et al. 2019; Ryu et al. 2020; Contarini et al. 2021).

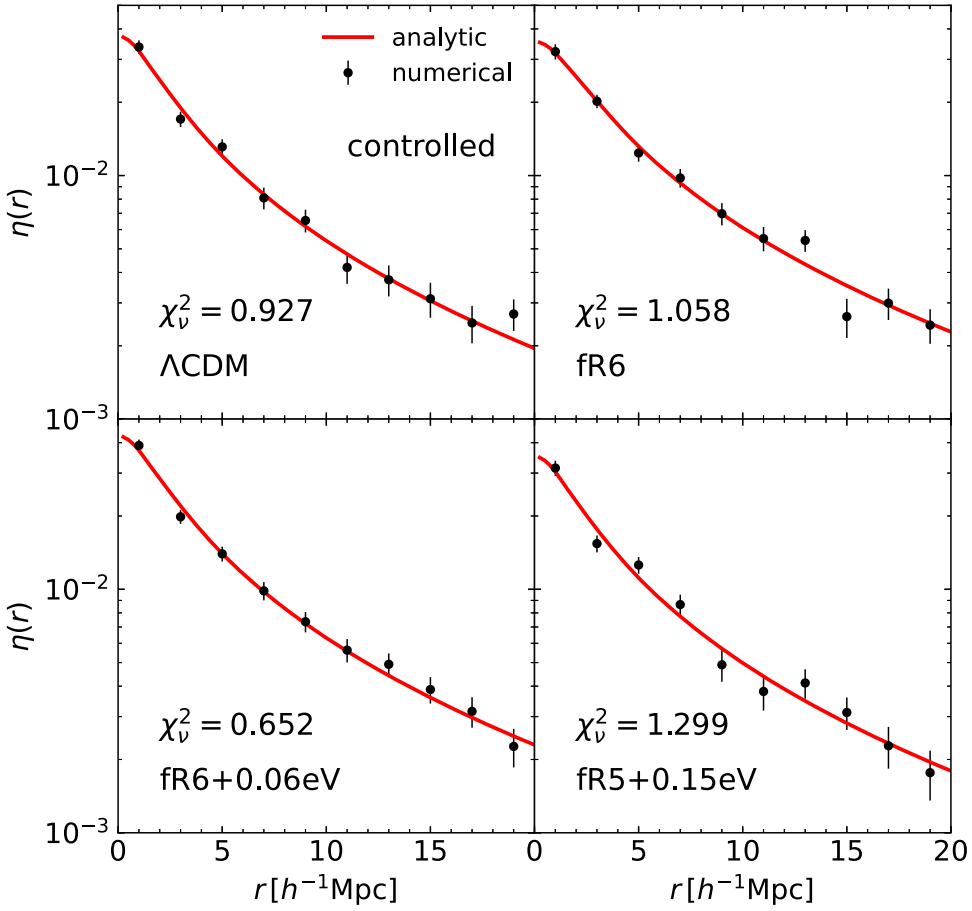

Figure 14. Same as Figure 6 but for the controlled samples.

Notwithstanding, our new diagnostics bear a couple of momentous limitations as cosmological discriminators they are to be applied to observational data. First, it is still quite difficult to determine the shape orientations of the group/cluster halos with high accuracy in practice, since what is readily measurable from the optical, X-ray emission, and Sunyaev–Zeldovich effect surveys (Boldt et al. 1966; Sunyaev & Zeldovich 1969; Sarazin 1988; Yee & Gladders 2002) is two-dimensional images of their baryonic components projected onto the plane of the sky, which themselves suffer from a nonlinear redshift-space distortion effect (Jackson 1972; Kaiser 1987; Hamilton & Hamilton 1998). Although complementary methods based on strong and weak gravitational lensing effects (Bartelmann 2010) are often used to measure directly the three-dimensional shapes of cluster halos, they can be applied only to very massive clusters with masses $\gtrsim 10^{15}\, h^{-1}\, M_\odot$ that can produce lensing signals strong enough to trace the dark matter distribution inside the clusters' virial radii (see Kneib & Natarajan 2011, for a review). For this reason, it would be highly desirable to model how the shape tracers of the group/cluster halos rather than their shapes themselves are spatially correlated and to investigate whether or not the tracer–tracer correlations can break the dark sector degeneracy. This investigation, however, would require us to examine first the dependence of the shape–tracer relation on the background cosmology. Besides, it would be much harder to find an analytic formula expressed in terms of the linear quantities for such tracer-tracer correlations, given that the shape tracers are expected to be nonlinearly biased (Harvey et al. 2021, and references therein).

The second limitation comes from the fact that our diagnostics are interdependent rather than independent of other diagnostics. In other words, although they can play a complementary role of distinguishing between any nonstandard cosmologies degenerate with the standard one whose initial conditions are all specified, they may not be powerful enough to constrain independently the key cosmological parameters themselves. Since the differences in the halo shape correlations among the νCDM+f(R) models might be reproduced by changes of the six cosmological parameters within the standard paradigm, it would be idealistic to explore how our diagnostics would behave in a much larger parameter space for an assessment of their true potential as a cosmological probe. Our future work will be in the direction of performing this more comprehensive work to overcome the limitations of our new diagnostics.

We are grateful to the anonymous referee whose constructive criticisms and many useful comments helped us to improve the original manuscript significantly. J.L. acknowledges the support of the Basic Science Research Program through the National Research Foundation (NRF) of Korea funded by the Ministry of Education (No.2019R1A2C1083855). M.B. acknowledges support from the project "Combining Cosmic Microwave Background and Large Scale Structure data: an Integrated Approach for Addressing Fundamental Questions in

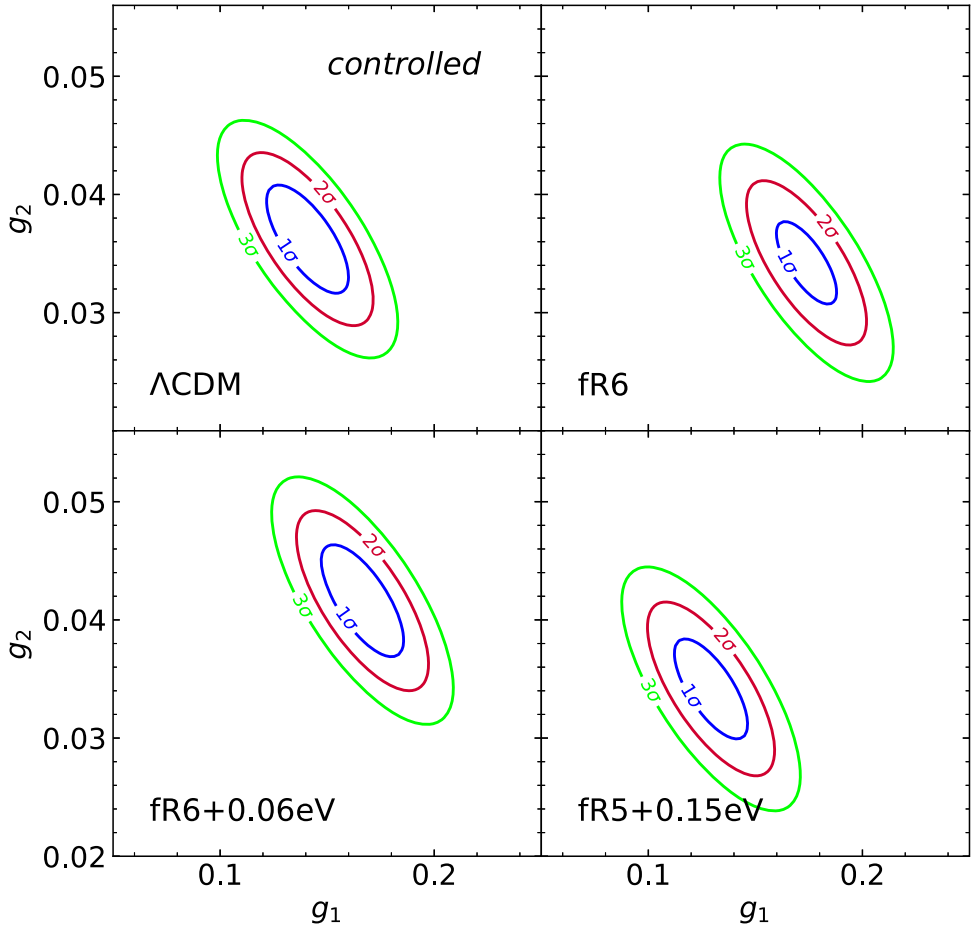

Figure 15. Same as Figure 7 but for the controlled samples.

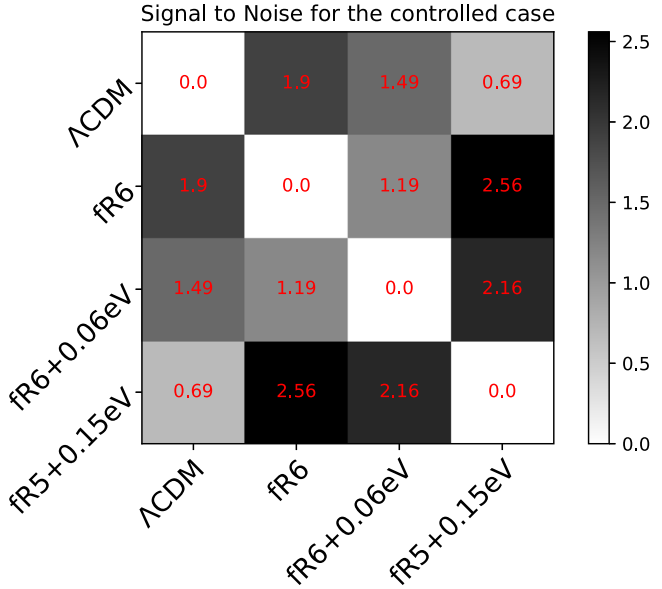

Figure 16. Same as Figure 8 but for the controlled samples.

Cosmology," funded by the MIUR Progetti di Ricerca di Rilevante Interesse Nazionale (PRIN) Bando 2017—grant 2017YJYZAH. M.B. also acknowledges the use of computational resources from the parallel computing cluster of the Open Physics Hub (https://site.unibo.it/openphysicshub/en) at the Physics and Astronomy Department in Bologna.

ORCID iDs

Jounghun Lee https://orcid.org/0000-0003-0522-4356
Marco Baldi https://orcid.org/0000-0003-4145-1943

References

Allgood, B., Flores, R. A., Primack, J. R., et al. 2006, MNRAS, 367, 1781
Altay, G., Colberg, J. M., & Croft, R. A. C. 2006, MNRAS, 370, 1422
Baldi, M., Villaescusa-Navarro, F., Viel, M., et al. 2014, MNRAS, 440, 75
Bartelmann, M. 2010, CQGra, 27, 233001
Behroozi, P. S., Wechsler, R. H., & Wu, H.-Y. 2013, ApJ, 762, 109
Blanchard, A., Héloret, J.-Y., Ilić, S., et al. 2022, arXiv:2205.05017
Boldt, E., McDonald, F. B., Riegler, G., & Serlernitsos, P. 1966, PhRvL, 21, 301
Boubekeur, L., Giusarma, E., Mena, O., et al. 2014, PhRvD, 90, 103512
Buchdahl, H. A. 1970, MNRAS, 150, 1
Carroll, S. M. 2001, LRR, 4, 1
Chen, S., Wang, H., Mo, H. J., et al. 2016, ApJ, 825, 49
Chuang, Y.-T., Okumura, T., & Shirasaki, M. 2022, MNRAS, 515, 4464
Contarini, S., Marulli, F., Moscardini, L., et al. 2021, MNRAS, 504, 5021
Faltenbacher, A., Gottlöber, S., Kerscher, M., et al. 2002, A&A, 395, 1
Giocoli, C., Baldi, M., & Moscardini, L. 2018, MNRAS, 481, 2813
Hagstotz, S., Costanzi, M., Baldi, M., & Weller, J. 2019, MNRAS, 486, 3927
Hagstotz, S., Gronke, M., Mota, D. F., et al. 2019, A&A, 629, A46
Hahn, O., Carollo, C. M., Porciani, C., & Dekel, A. 2007, MNRAS, 381, 41
Hamilton, D., & Hamilton, A. J. S. 1998, The Evolving Universe, Vol. 231 (New York: Springer International), 185
Harvey, D., Robertson, A., Tam, S.-I., et al. 2021, MNRAS, 500, 2627
Hu, W., & Sawicki, I. 2007, PhRvD, 76, 064004
Jackson, J. C. 1972, MNRAS, 156, 1
Kaiser, N. 1987, MNRAS, 227, 1
Kasun, S. F., & Evrard, A. E. 2005, ApJ, 629, 781
Khoury, J., & Weltman, A. 2004, PhRvD, 69, 044026

Kneib, J.-P., & Natarajan, P. 2011, A&ARv, 19, 47
Lee, J., & Pen, U.-L. 2001, ApJ, 555, 106
Lee, J., Springel, V., Pen, U.-L., & Lemson, G. 2008, MNRAS, 389, 1266
Lee, J. 2019, ApJ, 872, 37
Lee, J., Moon, J.-S., Ryu, S., et al. 2021, ApJ, 922, 6
Lee, J., & Moon, J.-S. 2022, ApJ, 936, 119
Li, B., & Barrow, J. D. 2007, PhRvD, 75, 084010
Libeskind, N. I., Hoffman, Y., Steinmetz, M., et al. 2013a, ApJL, 766, L15
Libeskind, N. I., Hoffman, Y., Forero-Romero, J., et al. 2013b, MNRAS, 428, 2489
Onuora, L. I., & Thomas, P. A. 2000, MNRAS, 319, 614
Peel, A., Pettorino, V., Giocoli, C., et al. 2018, A&A, 619, A38
Planck Collaboration, Ade, P. A. R., Aghanim, N., et al. 2016, A&A, 594, A24
Puchwein, E., Baldi, M., & Springel, V. 2013, MNRAS, 436, 348
Ryu, S., Lee, J., & Baldi, M. 2020, ApJ, 904, 93
Sarazin, C. L. 1988, Cambridge Astrophysics Series (Cambridge: Cambridge Univ. Press)
Smargon, A., Mandelbaum, R., Bahcall, N., & Niederste-Ostholt, M. 2012, MNRAS, 423, 856
Sotiriou, T. P., & Faraoni, V. 2010, RvMP, 82, 451
Starobinsky, A. A. 1980, PhRvB, 91, 99
Sunyaev, R. A., & Zeldovich, Y. B. 1969, Natur, 223, 721
Viel, M., Haehnelt, M. G., & Springel, V. 2010, JCAP, 2010, 015
Weinberg, S. 1989, RvMP, 61, 1
West, M. J. 1994, MNRAS, 268, 79
Wittman, D., Foote, D., & Golovich, N. 2019, ApJ, 874, 84
Wright, B. S., Koyama, K., Winther, H. A., et al. 2019, JCAP, 06, 040
Yee, H. K. C., & Gladders, M. D. 2002, in ASP Conf. Proc. 257, AMiBA 2001: High-Z Clusters, Missing Baryons, and CMB Polarization (San Francisco, CA: ASP), 109
Zaroubi, S., Squires, G., de Gasperis, G., et al. 2001, ApJ, 561, 600
Zhang, Y., Yang, X., Faltenbacher, A., et al. 2009, ApJ, 706, 747
Zhang, Y., Yang, X., Wang, H., et al. 2013, ApJ, 779, 160